



**HAL**  
open science

## Local climate zone approach on local and micro scales: Dividing the urban open space

Auline Rodler, Thomas Leduc

► **To cite this version:**

Auline Rodler, Thomas Leduc. Local climate zone approach on local and micro scales: Dividing the urban open space. *Urban Climate*, 2019, 28, pp.100457. 10.1016/j.uclim.2019.100457 . hal-02086327

**HAL Id: hal-02086327**

**<https://hal.science/hal-02086327>**

Submitted on 25 May 2021

**HAL** is a multi-disciplinary open access archive for the deposit and dissemination of scientific research documents, whether they are published or not. The documents may come from teaching and research institutions in France or abroad, or from public or private research centers.

L'archive ouverte pluridisciplinaire **HAL**, est destinée au dépôt et à la diffusion de documents scientifiques de niveau recherche, publiés ou non, émanant des établissements d'enseignement et de recherche français ou étrangers, des laboratoires publics ou privés.



Distributed under a Creative Commons Attribution - NonCommercial - NoDerivatives 4.0  
International License



38 is often higher in urban central districts than in their surrounding rural  
39 areas. This observation is called the **Urban heat island** and has a lot of  
40 consequences. **UHI** can increase the mortality risk, especially during heat  
41 waves. The lack of air circulation due to the urban heat island effect can  
42 influence the dispersion of air pollutants in a metropolis (Lai 2018). UHI  
43 can affect the outdoor comfort (Morille and Musy 2017) and energy con-  
44 sumption (Salvati, Coch Roura, and Cecere 2015).

45 Solutions are proposed to mitigate the UHI and lower the air tempera-  
46 ture in cities by:

- 47 • Increasing the albedo of materials to avoid the absorption of high amounts  
48 of solar radiation (Yu et al. 2008),
- 49 • Planting trees to create shadows and evapotranspiration (Santamouris  
50 et al. 2017),
- 51 • Covering roofs and facades with low vegetation (Musy, Malys, and  
52 Inard 2017),
- 53 • Pavement watering (Azam et al. 2018).

54 Urban morphology has proven to be useful to the understanding of the  
55 UHI and for the propagation of heat and cooling. For example, (Bernard,  
56 Rodler, et al. 2018) have highlighted that the cooling induced by a given  
57 park would better propagate within streets with a large aspect ratio (build-  
58 ing height to street width ratio, H/W).

59 The urban's morphology influence on the air temperature distribution  
60 in a built up area can be studied through climate models using the 2D/3D  
61 geometry of the city, such as **Solene-Microclimat** (Musy, Malys, Morille,  
62 et al. 2015), **ENVI-met**<sup>1</sup>). or previously developed climate models (Grim-  
63 mond et al. 2010). Urban climate modeling is usually performed on three  
64 scales (Tim R. Oke 2006; T. Oke 1987). On the mesoscale, a whole city can  
65 be studied, but local characteristics are parametrized and the results are ob-  
66 tained for homogenous cells, the dimension of which is generally  $\geq 200$  m.  
67 On the local scale, a district is extracted from its context and explicitly rep-  
68 resented, with building forms, materials, natural surfaces, etc. On the mi-  
69 croscale, very local phenomena are represented with an accurate level of  
70 detail aiming at representing trees, urban furnitures, etc. in a particular  
71 street.

72 Urban classification has been proposed to split the territory according  
73 to a Local Climate Zone (LCZ) definition (I. D. Stewart and T. R. Oke 2012).  
74 A local climate zone is a region of uniform surface cover, structure, mate-  
75 rial and human activity sizing hundreds of meters to several kilometers  
76 on a horizontal scale. Each LCZ is mainly governed by building height  
77 and spacing, pervious surface fraction, tree density and soil wetness (I. D.  
78 Stewart and T. R. Oke 2012; Iain D. Stewart, T. R. Oke, and Krayenhoff  
79 2014). Each LCZ has a characteristic screen-height temperature regime.  
80 LCZs can provide input data for numerical climate models that incorporate  
81 urban canopy parameters into their formulations to forecast the climatic  
82 conditions and UHI magnitudes. The applicability of the LCZ classifica-  
83 tion for different UHI study domains is proven by researchers (Leconte et  
84 al. 2015; Mills 2007; Perera and Emmanuel 2018; Geletič and Lehnert 2016;  
85 Kotharkar and Bagade 2018). Yet, it should be noted that a LCZ tempera-  
86 ture difference is not an urban-rural difference.

87 Most of the methods to find an appropriate LCZ are based on a process.  
88 Firstly, the territory is divided in meshes, or regular grids, and the relevant

---

<sup>1</sup><https://www.envi-met.com/> (Accessed February 2019).

89 data is collected. Secondly, the thermal source area of the station is esti-  
90 mated. Thirdly, the geometric and surface cover properties are calculated  
91 within each mesh from vector databases or satellite images if provided. Fi-  
92 nally, each mesh is linked to a LCZ. These steps have been mostly done  
93 manually (Leconte et al. 2015), but some authors propose automatic solu-  
94 tions (Bocher et al. 2018; Lelovics et al. 2014).

95 Standardized and automatic methods to calculate urban indicators and  
96 to classify the urban fabric for any city in the world is nowadays a chal-  
97 lenge. The World Urban Database and Access Portal Tools (WUDAPT)  
98 is a community-based project with the scientific aim to classify the urban  
99 fabric (on the city scale) by climate properties from available data at on a  
100 world scale, using free satellite images and free and open-source software  
101 such as the SAGA Geographic Information System (GIS). Most of the stud-  
102 ies using the LCZ approach classify entire cities or megalopolises and use  
103 large grids<sup>2</sup>: WUDAPT community calculates LCZs with resolutions rang-  
104 ing from 300 m to 10 km.

105 However, it is possible to study the LCZs at a finer scale (Quanz et al.  
106 2018). For example, we know that the building density, the sky view fac-  
107 tor and surface cover are not uniform in any LCZ, and thus temperatures  
108 fluctuate across short distances (Iain D. Stewart, T. R. Oke, and Krayenhoff  
109 2014). Remarkable spatial variability of air temperature in a LCZ was ob-  
110 served during short-term observations (Leconte et al. 2015) and long-term  
111 observations (Fenner et al. 2017). The inter-LCZ differences seem to be  
112 especially pronounced at night-time and present between inner-city LCZ  
113 (Fenner et al. 2017), which leads the authors to say that the LCZ classifica-  
114 tion method should be improved to derive LCZ sub classes. These observa-  
115 tions lead us to use the LCZ approach on smaller parts of a city. However,  
116 few works so far have investigated intra-urban LCZs.

117 Results are influenced by both the shape and scale of the aggregation  
118 unit, as pointed out by the Modifiable Areal Unit Problem (Openshaw  
119 1983). Available maps generated by the Urban planning and Layouts agency  
120 for the Ile-de-France region show that the zoning is made of contiguous ur-  
121 ban blocks surrounded by streets. Some authors (Plumejeaud-Perreau et al.  
122 2015) raised a problem linked to this zoning method: "the produced zoning  
123 is not a continuous one: the set of cells do not build a full partition of the  
124 urban space". A solution exists, based on the union of contiguous cadastral  
125 parcels: the frontiers of islets are built so as to share in two parts the space  
126 existing between each street-block. For that purpose, some researchers in  
127 urban planning and architecture (Plumejeaud-Perreau et al. 2015; Sarradin  
128 et al. 2007) use the properties of skeleton tessellation for a balanced zoning  
129 between a set of points or 'virtual sensors'.

130 Finally, the main contributions of this paper are:

- 131 • First, a fine grain formalism of the LCZ classification by using 2D-GIS  
132 with standard (vector) datasets. Five indicators are implemented and  
133 the LCZ approach used. A vector database is used to transpose results  
134 into computer-aided design tools. Among the implemented indica-  
135 tors, the aspect ratio is improved by implementing two equations for  
136 the squares and the streets, and the sky view factors is adapted from  
137 (Bernard, Bocher, et al. 2018).
- 138 • Second, a detailed street-level implementation of five indicators such  
139 as Sky View Factor, aspect ratio, Building Surface Fraction, Impervi-  
140 ous Surface Fraction, and Height of Roughness Elements. These five

---

<sup>2</sup><http://www.wudapt.org/> (Accessed February 2019).

141 indicators, coupled with the intervals provided by (I. D. Stewart and  
142 T. R. Oke 2012), make it possible to estimate the LCZ of the immediate  
143 environment of any sensor. By aggregation, we can deduce the LCZ  
144 on the block - or district scales.

- 145 • Third, a space meshing method to improve computation times while  
146 ensuring correlation to the LCZs found is studied. Indeed, the skele-  
147 tonization of the unbuilt space allows to decimate the number of sen-  
148 sors, compared to a network of irregular triangles obtained by Delau-  
149 nay triangulation.
- 150 • Fourth, the observation that the intervals proposed by (I. D. Stewart  
151 and T. R. Oke 2012) are not perfectly covering all the potential indicator  
152 values (insofar as they do not allow any type of fabric to be classified  
153 in one of the seventeen LCZs provided by (I. D. Stewart and T. R. Oke  
154 2012)).

155 This paper is structured as follows. First, the materials and methods are  
156 presented (including the LCZ classification, the several indicators, and the  
157 global methodology implemented). Second, the results are shown on three  
158 different districts. Finally, the discussion and conclusion close the paper.

## 159 2 Materials and **methods**

### 160 2.1 LCZ classification

161 As a reminder, the LCZs are defined as "regions of uniform surface  
162 cover, structure, material, and human activity that span hundreds of me-  
163 ters to several kilometers in horizontal scale" (I. D. Stewart and T. R. Oke  
164 2012). The LCZ concept classifies urban and natural environments into  
165 classes characterized by geometric, surface parameters, thermal, radiative  
166 and metabolic properties for local climate zones. Each LCZ has a specific  
167 range of these parameters and the ones used in this paper are presented  
168 in Table 1. The concept distinguishes between ten "urban" or "built-up"  
169 and seven "natural" LCZs (Fig. 1). In this paper, the thermal, radiative and  
170 metabolic properties of each urban component are not used as they are  
171 missing data. Moreover, of the seven indicators proposed by (I. D. Stewart  
172 and T. R. Oke 2012), two are not implemented for very different reasons.

- 173 • For our **dataset**, the terrain's roughness class does not discriminate on  
174 the chosen scale level.
- 175 • Due to the lack of availability of appropriate **datasets** (e.g. grassy back-  
176 yards are not listed in the topographic repositories available to us), the  
177 Pervious Surface Fraction cannot be properly implemented.

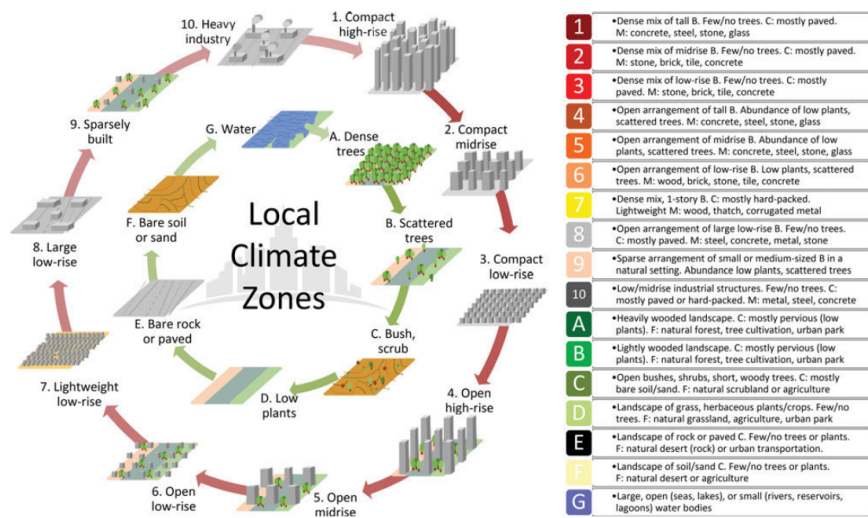


**Fig. 1:** Local climate zone concept with 'urban' LCZ (1-10) and 'natural' LCZ (A-G); icons reworked. B: buildings, C: cover, M: materials, F: function, tall: > 10 stories, mid-rise: 3-9 stories, low: 1-3 stories. Figure taken from (Bechtel et al. 2017).

Table 1: Values of geometric and surface cover properties for local climate zones. All properties are unit-less except the height of roughness elements (meters) (I. D. Stewart and T. R. Oke 2012).

Local Climate Zone (LCZ)	Sky view Factor	Aspect Ratio	Building surface fraction	Impervious surface fraction	Height of roughness elements
LCZ 1 Compact high-rise	0.2-0.4	> 2	40-60	40-60	> 25
LCZ 2 Compact midrise	0.3-0.6	0.75-2	40-70	30-50	10-25
LCZ 3 Compact low-rise	0.2-0.6	0.75-1.5	40-70	20-50	3-10
LCZ 4 Open high-rise	0.5-0.7	0.75-1.25	20-40	30-40	> 25
LCZ 5 Open midrise	0.5-0.8	0.3-0.75	20-40	30-50	10-25
LCZ 6 Open low-rise	0.6-0.9	0.3-0.75	20-40	20-50	3-10
LCZ 7 Lightweight low-rise	0.2-0.5	1-2	60-90	< 20	2-4
LCZ 8 Large low-rise	> 0.7	0.1-0.3	30-50	40-50	3-10
LCZ 9 Sparsely built	> 0.8	0.1-0.25	10-20	< 20	3-10
LCZ 10 Heavy industry	0.6-0.9	0.2-0.5	20-30	20-40	5-15
LCZ A Dense trees	< 0.4	> 1	< 10	< 10	3-30
LCZ B Scattered trees	0.5-0.8	0.25-0.75	< 10	< 10	3-15
LCZ C Bush, scrub	0.7-0.9	0.25-1	< 10	< 10	< 2
LCZ D Low plants	> 0.9	< 0.1	< 10	< 10	< 1
LCZ E Bare rock or paved	> 0.9	< 0.1	< 10	> 90	< 0.25
LCZ F Bare soil or sand	> 0.9	< 0.1	< 10	< 10	< 0.25
LCZ G Water	> 0.9	< 0.1	< 10	< 10	-

## 178 2.2 Data sources

179 For reasons of replicability, we have decided to use standard topographic  
180 **datasets** and software. To guarantee this deliberate choice, we have identified  
181 the European INSPIRE directive for the two sites we have selected  
182 in France. This Directive, which entered into force on 15 May 2007, aims  
183 to create a European Union spatial data infrastructure to facilitate and promote  
184 EU policies and activities that may have an impact on the environment.  
185

186 For the French case, the BD TOPO® database, which is a 3D vectorial  
187 description (structured in objects) of the elements of the territory and its  
188 infrastructures, of metric precision, usable on scales ranging from 1:5,000  
189 to 1:50,000, complies with the recommendations of the INSPIRE directive.

190 This topographic database, which consistently covers the entire national  
191 territory, is made available by the IGN. Its data and technical specifications

192  
193  
194  
195  
196  
197  
198  
199  
200  
201  
202  
203  
204  
205  
206  
207  
208  
209  
210  
211  
212  
213  
214  
215  
216  
217  
218

are published and available online<sup>3</sup>.

In order to test and validate our approach with a non-European dataset, we have identified an urban fragment on the North American territory. The planimetric dataset available for free for the NYC OpenData portal seemed to us to be the most immediately usable. This data is derived from the imaging products delivered with the New York State Overview in 2014. It includes a set of polygonal building footprints representing the perimeter contour of each building. These geometries are completed with attributes such as the height of the roof above the ground elevation. Corresponding data and technical specifications are published and available online<sup>4</sup>. Concerning the geometry of the street network, we use polylines from the New York Citywide Street Centerline database, a single line representation of New York City streets. Corresponding data and technical specifications are published and available online<sup>5</sup>.

To test this new approach, we have selected three case studies with very different morphologies, presenting various architectural styles. The aim was also to test different types of **datasets**, in order to have a more robust method. The first is a typical urban configuration of a North American city with contemporary architecture. It is an area of about 73.7 ha located in Borough Park, Brooklyn, New York (40.7128°N, 74.0060°W). The second and third cases are located in Nantes (47.2184°N, 1.5536°W), a medium-sized city in the west of France. The second case (which we call the "Royale district") is an urban centre of about 11.3 ha composed of a homogeneous set of buildings that reflect the classical architecture of the 18<sup>th</sup> and 19<sup>th</sup> centuries. The third case (which we call "Méthode district") is a residential area of intermediate density. It is a mixed sector of about 12.7 ha, composed of single-family homes, as well as large housing buildings.

219  
220

## 2.3 Implementation of urban indicators: geometric and surface cover properties

221  
222  
223  
224  
225

For the determination of the LCZs, we have chosen to evaluate the several indicators mentioned in Table 1 in a set of points that we call "virtual sensors". The objective of this section is to present the details of the implementation of indicators by first introducing some key concepts. We will be concerned with the location of these virtual sensors in the next section.

226  
227

### 2.3.1 Prerequisites: delimit the boundaries of the immediate surroundings

228  
229  
230  
231  
232  
233  
234  
235  
236

Lets consider a virtual sensor (represented by a red dot on Fig. 2, Fig. 3, and Fig. 7). In order to calculate the above-mentioned indicators at this point, we start by introducing two different methods for determining the immediate environment of the corresponding position.

The first method, very classic, is a circular buffer, whose radius length is arbitrarily chosen (see Fig. 2a). It can be estimated that, because it does not take into account the presence of possible masks in the area (masks likely to alter the physical phenomenon under study), this buffer characterizes isotropic phenomena, i.e. identically distributed in all directions of space.

<sup>3</sup>At <http://professionnels.ign.fr/bdtopo> (Accessed February 2019).

<sup>4</sup>At [https://github.com/CityOfNewYork/nyc-geo-metadata/blob/master/Metadata/Metadata\\_BuildingFootprints.md](https://github.com/CityOfNewYork/nyc-geo-metadata/blob/master/Metadata/Metadata_BuildingFootprints.md) (Accessed February 2019).

<sup>5</sup>At [https://github.com/CityOfNewYork/nyc-geo-metadata/blob/master/Metadata/Metadata\\_StreetCenterline.md](https://github.com/CityOfNewYork/nyc-geo-metadata/blob/master/Metadata/Metadata_StreetCenterline.md) (Accessed February 2019).

237 The second method, less frequently used, is called the isovist, a notion  
 238 that has been theorized by (Benedikt 1979). It corresponds to all the points  
 239 of the plane directly "visible" from a given location, in all directions (it is  
 240 a panoptic feature), integrating the notion of "mask", such as built masks  
 241 for example (see Fig. 2b). In outdoor spaces, the isovist is almost systematic-  
 242 ally associated with an artificial horizon, which prevents "the rays from  
 243 starting infinitely" (see Fig. 2b, the western part of the isovist is truncated  
 244 by the circular buffer of a 200 m radius assimilated to an artificial horizon).  
 245 With a standard topographic dataset, this isovist is a polygonal surface in a  
 246 horizontal plane. It is very useful to define and qualify the open space that  
 247 immediately surrounds the observation/generation point.

248 The immediate environment of the virtual sensor having been defined,  
 249 we introduce a second tool in order to be able to characterize it. This is a  
 250 transposition of the ray-casting mechanism to the GIS context (see Fig. 3a).  
 251 This involves launching a set of rays, equidistributed in all directions of  
 252 the plane (which implies that the pitch of the corresponding angular abscissa  
 253 is  $\frac{2\pi}{nRays}$ ). For a given direction, the corresponding radius strikes a group  
 254 of buildings. Depending on the indicator chosen, we can either select the  
 255 pair  $(h[i], w[i])$  corresponding to the smallest  $w[i]$  (this is the solution used  
 256 to calculate the aspect ratio) or the pair  $(h[i], w[i])$  that maximizes the ratio  
 257  $\frac{h[i]}{w[i]}$  (this is the solution used to calculate the sky view factor), as shown in  
 258 Fig. 3b.



Fig. 2: Two different methods of delineating surrounding spaces: (a) Circular buffer. (b) Isovist.

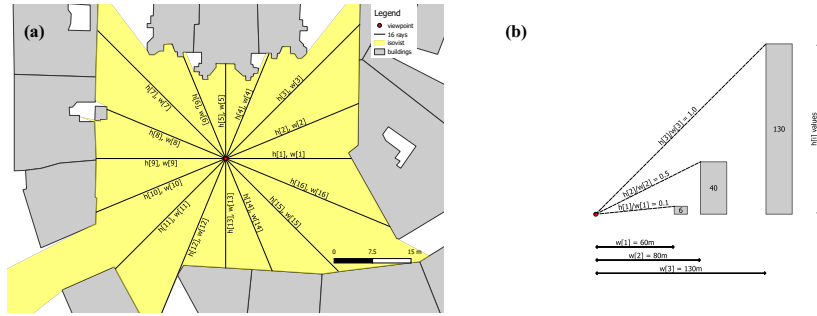


**Fig. 3:** (a) Ray cast strategy: Set of rays casted from a given position with corresponding  $w[k]$  (ray length from the position to the hitting point on building) and  $h[k]$  (building height) attributes. Buildings elevations are inscribed in the corresponding building's footprints. (b) For a given direction, the corresponding radius strikes a group of buildings. Depending on the indicator chosen, we can either select the pair  $(h[i], w[i])$  corresponding to the smallest  $w[i]$  or the pair  $(h[i], w[i])$  that maximizes the ratio  $\frac{h[i]}{w[i]}$ .

### 259 2.3.2 Sky view factor (SVF)

260 The sky view factor is an indicator of the amount of sky vault visible  
 261 from the ground at a given position, i.e. the proportion of sky not ob-  
 262 structed by the surrounding built masks. Several calculation methods exist  
 263 based on the analysis of fisheye-lens photographs (Steyn 1980), empirical  
 264 laws on simplified street models (Johnson and Watson 1984), double pro-  
 265 jection mechanisms and sky opening maps (Teller and Azar 2001), digital  
 266 vector approaches (Souza, Rodrigues, and Mendes 2003), and raster-based  
 267 approaches (Gál, Lindberg, and Unger 2009).

268 Because our case studies are urban fragments of a few hundred square  
 269 meters and because we need an inframetric resolution (as we will see later  
 270 in the section dedicated to partitioning the unbuilt space), we have opted  
 271 for a vector implementation of the SVF by adapting (Bernard, Bocher, et al.  
 272 2018). This approach has the advantage of being more precise than raster-  
 273 based implementations and not dependent on the way the selected space  
 274 is divided.

Lets consider  $(r, \theta, \varphi)$  the spherical coordinates of a given point, where  $r$   
 is the Euclidean radial distance to the origin,  $\theta$  is the latitude to the equator  
 plane, and  $\varphi$  is the azimuthal angle (longitude) starting from east. With  
 these notations, the spherical surface element ranging from  $\theta$  to  $\theta + d\theta$  and  
 from  $\varphi$  to  $\varphi + d\varphi$  on a spherical surface at constant radius  $r$  is:

$$d^2S = r^2 \cos(\theta) d\theta d\varphi \quad (1)$$

And the corresponding differential solid angle is equal to:

$$d\Omega = \cos(\theta) d\theta d\varphi \quad (2)$$

If we integrate this differential solid angle on the spherical surface in  
 red in Fig. 4a, we obtain the following equation (after dividing the hemi-  
 sphere equally into slices by rotation angle  $\frac{2\pi}{nRays}$ ):

$$\Omega_i = \int_{\varphi=0}^{\frac{2\pi}{nRays}} \int_{\theta=0}^{\arctan(\frac{H_i}{W_i})} \cos(\theta) d\theta d\varphi = \frac{2\pi \times \sin(\arctan(\frac{H_i}{W_i}))}{nRays} \quad (3)$$

In the case of Fig. 4b, the ratio of visible sky divided by the surface of a unit hemisphere ( $2\pi$  sr) is therefore equal to the complementary to the sum of the solid angles of the various surrounding built masks and equal to:

$$\text{SVF} = \frac{2\pi - \sum_{i=0}^{\text{nRays}} \Omega_i}{2\pi} = 1 - \frac{1}{\text{nRays}} \sum_{i=1}^{\text{nRays}} \sin(\arctan(\frac{H_i}{W_i})) \quad (4)$$

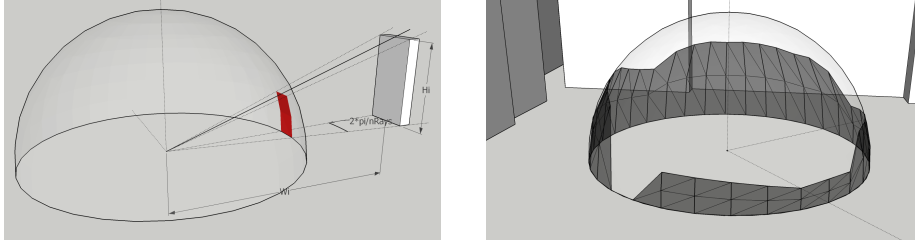


**Fig. 4:** (a) The solid angle of the built mask of height  $H_i$ , angular deviation  $\frac{2\pi}{\text{nRays}}$ , located at the distance  $W_i$  from the point of view is equal to  $\frac{2\pi}{\text{nRays}} \sin(\arctan(\frac{H_i}{W_i}))$ . (b) The sky view factor is the ratio of the amount of the sky hemisphere visible from the ground to that of an unobstructed hemisphere.

275 As mentioned in the previous section, in the specific context of the eval-  
 276 uation of the SVF, in order to calculate the solid angle of the built mask rep-  
 277 resented in Fig. 4a, we select the pair  $(h[i], w[i])$  that maximizes the ratio  
 278  $\frac{h[i]}{w[i]}$  (see Fig. 3b).

### 279 2.3.3 Aspect ratio (H/W)

280 In the simplified city model developed by (T. Oke 1988), the street canyon  
 281 is the basic geometric unit that allows, by simple repetition, to approximate  
 282 the urban fragment studied. If we make the (strong) assumption that the  
 283 buildings flanking this street canyon are infinite in length, then this model  
 284 can be simplified by a two-dimensional cross-section. This very simplified  
 285 configuration makes it possible to introduce  $h/w$  the aspect ratio, as the ra-  
 286 tio of the average height of the canyon walls ( $h$ ) to the width of the canyon  
 287 ( $w$ ).

288 We propose to extend this definition to squares and other open spaces  
 289 that are clearly not comparable to canyons. To this end, and provided that  
 290 we are able to discriminate between urban canyons and other open spaces,  
 291 we use the aforementioned ray casting method. When the viewpoint is  
 292 located in a street canyon, a pair of "directional" rays are casted towards  
 293 the nearest buildings. On the other hand, when the viewpoint is located in  
 294 a space that is not considered a street canyon, a collection of panoptic rays  
 295 (equidistributed in all directions of the plane) is casted. Indeed, in the case  
 296 of a more widely open space, no main orientation can be easily identified in  
 297 contrast with the case of canyon street. This dual implementation is shown  
 298 in Fig. 5. The following formula is a generalization of the aspect ratio that  
 299 is valid in both cases.

$$\text{aspect ratio} = \frac{\frac{1}{\text{nRays}} \sum_{i=0}^{\text{nRays}} h_i}{\frac{1}{\text{nRays}} \sum_{i=0}^{\text{nRays}} 2 \times w_i} = \frac{\bar{h}}{2 \times \bar{w}} \quad (5)$$

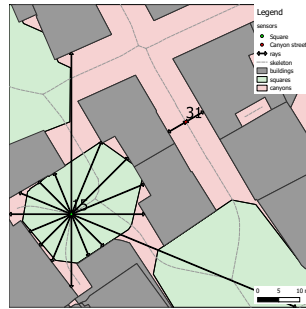


**Fig. 5:** To calculate the aspect ratio, we use two different methods, depending on the position of the sensor. When located in a canyon street (point #31), the ray cast is "directional" (meaning that it is thrown towards the nearest building). When the sensor is located in a square (point #15), the ray cast is panoramic.

300 To detect and identify the squares and canyon streets, the traditional  
 301 dilation-erosion technique is adopted. The first step consists in homo-  
 302 geneous dilation (uniform expansion in all directions of the plane) of all  
 303 building footprints using the same arbitrarily fixed buffering distance. This  
 304 enlargement is followed by a spatial union that allows for fusion of nearby  
 305 building footprints (see Fig. 6a). The next step is to apply homothetic re-  
 306 duction to all the extended building footprints resulting from the previ-  
 307 ous space union. These "eroded" built spaces are then subtracted from the  
 308 study area to delineate so-called "squares" or large open spaces. These ur-  
 309 ban squares are the result of a fourfold process of dilation, merging, erosion  
 310 and subtraction (see Fig. 6b). Once the squares have been identified, the fi-  
 311 nal step is to delineate the urban canyons. It is a two-step operation. By  
 312 subtracting the buildings from the study area, we obtain all open or unbuilt  
 313 spaces (like some sort of photochemical negative in the silver photographic  
 314 transform). All that remains is then to remove the several squares identi-  
 315 fied in the previous step to delineate the streets canyons (Fig. 6c).

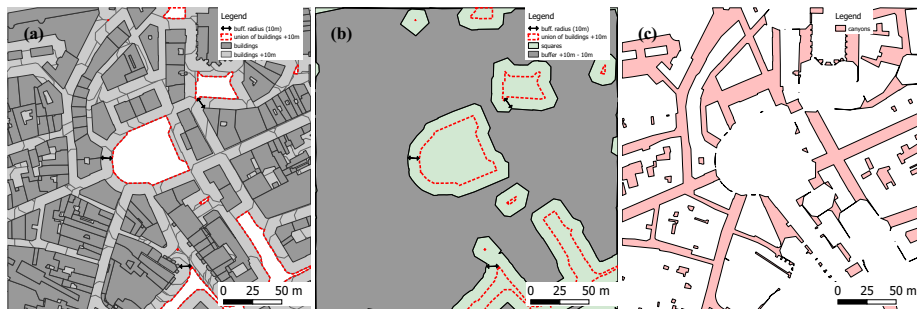


**Fig. 6:** Use of a dilation-erosion technique for the automatic detection of canyon streets and squares. In this example, the street width parameter is arbitrarily set to 10 m. (a) Buildings dilation, street canyons disappear. (b) Erosion of "extended" buildings (by spatial union), squares identification. (c) Identification of canyon streets (by subtracting squares from all open spaces).

316

### 2.3.4 Building surface fraction (BSF)

317

The building surface fraction is a dimensionless indicator that represents, for a given reference area, the ratio of built area. To calculate it, we start by adding the areas of the different building footprints (or portions of building footprints) included in the circular buffer area shown in Fig. 2a. The BSF is equal to the ratio of this cumulative area divided by the disk area of the circular buffer mentioned above.

322

323

### 2.3.5 Impervious surface fraction (ISF)

324

To calculate the impervious surface fraction, we must first reconstruct the shape of the impervious cover as accurately as possible. This reconstruction is the result of a homothetic dilation of the road centerlines provided by input datasets. It also depends on the width of each road segment. Which is an attribute of the corresponding layer (namely "LARGEUR" within the BD TOPO®, and "st\_width" within the New York Citywide Street Centerline database). Fig. 7 shows an application of this virtual reconstruction of the road surface in the case of New York terrain.

325

326

327

328

329

330

331

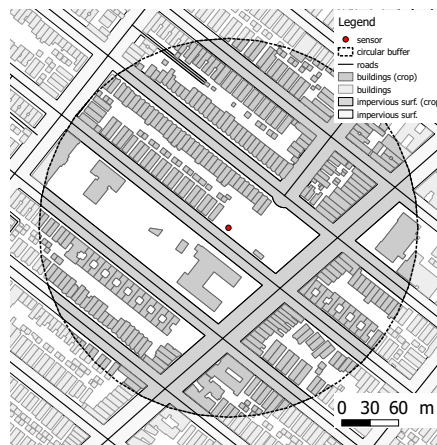


Fig. 7: Systematic application of a buffer on road centerlines (the "st\_width" buffering distance varies from 8 ft, to 30, and even 48 on the main road).

332

### 2.3.6 Height of roughness elements (HRE)

333

The height of roughness elements or absolute roughness is the mean height of the urban canopy. For a given reference area (the circular buffer shown in Fig. 2a), it is equal to the sum of the surfaces of the building footprints (or portions of building footprints) included in the reference zone, multiplied by the respective building heights and divided by the total reference area.

334

335

336

337

338

339

## 2.4 Positioning of sensors

340

Our objective is to qualify the LCZ at any point on the ground, based on the calculation of the various morphological indicators mentioned above, and, by grouping these elementary units contiguously, to define uniform subdivisions - in the climatic sense - of space. The study space (which is

341

342

343

344 limited to urban open spaces only) being continuous, the first step consists  
 345 in its discretization. Several solutions exist, such as, for example, a regular  
 346 grid of the space (Fig. 8a), a Delaunay triangulation of the space (Fig. 8b),  
 347 or a skeletonization of the space (Fig. 8c).

348 The regular grid is presented as it is still used in some approaches. The  
 349 drawback with this grid is that it is unsuitable for a real city geometry and  
 350 favours cardinal orientations. A regular grid does not accurately represent  
 351 a sloped surface unless it is meshed very thinly. For this reason the calcu-  
 352 lations will not be undertaken on the regular grid.

353 If the triangulation discretization approach has the advantage of be-  
 354 ing perfectly covering, it must be noted that it excessively multiplies the  
 355 number of triangles and, consequently, of virtual sensors. The third ap-  
 356 proach by open space skeletonization is a repetition of a technique com-  
 357 monly used in shape analysis (from cartographic generalization to optical  
 358 character recognition). The technique used is derived from the Voronoi  
 359 diagram. It allows, by dimensional reduction, to cover the shape in its  
 360 complexity with a small number of virtual sensors (these sensors being de-  
 361 rived from the discretization by curvilinear abscissa of the skeleton). The  
 362 question that arises, however, is the relevance of this alternative proposal  
 363 in the sense of LCZs zoning.

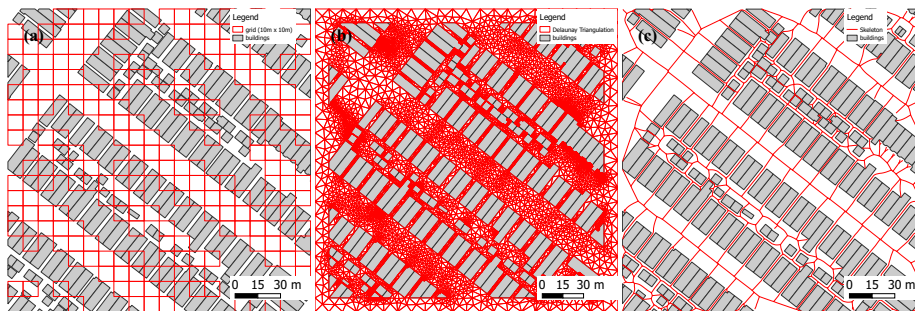


Fig. 8: Three different methods of dividing space: (a) Regular grid (217 cells). (b) Triangulated Irregular Network (TIN) based on a constrained Delaunay Triangulation (11,288 triangles). (c) Skeleton (defined as the set of centers of all maximal disks inscribed in the non-built space, cumulative length of 4,6 km).

## 364 2.5 LCZs match-making

### 365 2.5.1 Nearest neighbour

366 To study the validity of the skeleton-based approach, we will compare  
 367 the LCZ zoning resulting from triangulation (exhaustive coverage of space)  
 368 with the zoning associated with the skeleton. It is a two-step process. The  
 369 first consists in match-making, through a spatial joint to the nearest neigh-  
 370 bour, each virtual sensor associated with triangulation to the nearest virtual  
 371 sensor resulting from skeleton sampling. This grouping having been carried  
 372 out, we proceed to an average calculation in a second step. Indicator  
 373 by indicator and by grouping sensors from triangulation (associated with  
 374 the same skeleton sensor), we perform an arithmetic average. The LCZ as-  
 375 sociated with the sensor group is the one deduced from Table 1 using these  
 376 different average values.

377

## 2.5.2 Major, minor, and LCZ determination

378

Whether it is to assign a LCZ class to a virtual sensor from the Delaunay triangulation, a virtual sensor from skeletonization, or a "medium" virtual sensor representing a group of virtual sensors (cf. the nearest neighbour process described before), the process is identical.

379

380

381

382

383

384

385

386

387

388

389

390

391

392

It seems nearly impossible to find for each sensor a LCZ, and often not only one LCZ is found. That is why subclasses among the LCZs can be proposed (I. D. Stewart and T. R. Oke 2012). To apply the same data processing on all sensors, an algorithm to find the major and minor LCZs is proposed and adopted here. The LCZ attribute associated with each virtual sensor is similar to a collection of labels, where each label is a two-letter word composed of a "major" and a "minor". The major one, which is the first letter of the word, corresponds to a strong determination (5 out of 5 indicators belong to the associated LCZ, as defined in Table 1). The minor, which is the second letter of the word, corresponds to a weak determination (only 4 of the 5 indicators belong to the associated LCZ as defined in Table 1).

393

394

395

396

397

398

399

400

In the case of the Nantes - Royale application that we will present in the following article, 9 sensors (out of 15,316) are labelled "02#03" in terms of LCZ. This label shows that, for these sensors, there is no strong determination (0 as a major), but that, on the other hand, two weak determinations are possible. Therefore, these sensors belong to classes 2 and 3 alike. We can consider that they are positioned at some sort of transition points. The sharp sign separates several identified LCZs having the same weight for a given sensor.

401

## 2.5.3 LCZ matching in details

Lets consider  $LCZ_1$  and  $LCZ_2$  be two labels (collection of labels or of 2-character words) to match. Lets note  $M_1$  (respectively  $M_2$ ) the set of majors of  $LCZ_1$  (respectively  $LCZ_2$ ) and  $m_1$  (respectively  $m_2$ ) the set of minors of  $LCZ_1$  (respectively  $LCZ_2$ ), then:

$$LCZ_1 = (M_1, m_1) \tag{6}$$

and

$$LCZ_2 = (M_2, m_2) \tag{7}$$

402

With this encoding, the LCZ of label "02#03" is written:  $LCZ_{02\#03} = (\{\}, \{2, 3\})$ .

403

The indeterminacy character "0" is not transcribed.

404

405

406

407

Table 2 lists a similarity measure for each given LCZ encoding pair. The larger the confidence index is and the closer the encodings are; the weaker it is and the more the encodings differ. This measure of similarity is renamed the "confidence index".

Table 2: Values of the confidence index as a function of LCZs. The instructions in this table are to be processed in order (starting from the first line to the default condition on the last line).

#Rule	Condition for the comparison of LCZ <sub>1</sub> and LCZ <sub>2</sub>	Confidence index
1	$M_1 = M_2$ and $m_1 = m_2$	100%
2	$M_1 \cup m_1 = M_2 \cup m_2$	80%
3	$M_1 = M_2$ and $m_1 \subset m_2$ and $m_1 \neq \{\}$	70%
4	$M_1 = M_2$ and $m_2 \subset m_1$ and $m_2 \neq \{\}$	70%
5	$M_1 = M_2$ and $m_1 \cap m_2 \neq \{\}$	60%
6	$(M_1 \cup m_1) \subset (M_2 \cup m_2)$ and $(M_1 \cup m_1) \cap (M_2 \cup m_2) \neq \{\}$	50%
7	$(M_2 \cup m_2) \subset (M_1 \cup m_1)$ and $(M_1 \cup m_1) \cap (M_2 \cup m_2) \neq \{\}$	50%
8	$M_1 = M_2$	30%
9	$M_1 \cap M_2 \neq \{\}$ and $m_1 = m_2$	20%
10	$m_1 = m_2$	10%
11	...	0%

408 For example, according to rule number 7, the confidence index associ-  
409 ated with the comparison of the labels "02#03" and "30" is 50%.

## 410 2.6 Methodology

411 The workflow presented in Fig. 9 is the one we implemented. It is di-  
412 vided into three groups of tasks: those related to pre-processing, those re-  
413 lated to processing and finally those related to post-processing. The main  
414 core of this workflow corresponds to tasks labelled from 2 to 10. As may  
415 be noticed, this main core is branched to tasks 4 and 6 on the one hand,  
416 and 5 and 7 on the other. In fact, the objective is to study the influence of  
417 the sampling solution (Delaunay triangulation vs. Skeletonization) on the  
418 accuracy of LCZs found and the respective calculation times. Therefore, a  
419 sensitivity study to the "sampler" was undertaken. We adopted the most  
420 common approach, that is, changing one-factor-at-a-time and evaluating  
421 the induced effect on the output.

### 422 2.6.1 Preprocessing (tasks 1, 2, 3, and 8)

423 The purpose of the preprocessing phase is to prepare: a) the calculation  
424 of the **aspect** ratio indicator (task 1), b) the determination of the study area  
425 that we will sample in order to position the indicators (tasks 2 and 3), and  
426 c) the calculation of the Impervious Surface Fraction indicator (task 8).

427 In the first case, we distinguish street canyons from other open spaces  
428 using a dilation-erosion method already mentioned (task 1). In the second  
429 case (task 2), we first produce the open space to be studied by subtracting  
430 building footprints from the entire study area (also called the region of  
431 interest, roi). Then, the objective of task 3 is to simplify the contours of  
432 this potentially complex geometric shape. Finally, in the third case, we  
433 delineate road surfaces (impervious) by dilating the road centerlines (task  
434 8).

### 435 2.6.2 Processing (tasks 4, 5, 6, 7, and 9)

436 Two concurrent sets of tasks structure the processing. The first aims  
437 to sample the open space under study from its skeleton. Therefore, task

438 4 allows to produce this skeleton using a Voronoi diagram. Task 6 gen-  
439 erates the collection of virtual sensors resulting from curvilinear abscissa  
440 sampling of the polyline corresponding to the skeleton.

441 The second group of tasks aims to sample the open space under study  
442 from a network of irregular triangles. Therefore, task 5 is responsible for  
443 producing this network using a Delaunay triangulation, while task 7 con-  
444 sists of identifying all the associated virtual sensors (as centroids of the  
445 mesh items).

446 Finally, task 9 is the one that, for the two sets of virtual sensors resulting  
447 from tasks 6 and 7, is dedicated to the calculation of the 5 indicators already  
448 presented and the resulting LCZ classification.

### 449 **2.6.3 Post-processing (task 10)**

450 Post-processing is summarized in task 10. It consists of a) a spatial  
451 joint to the nearest neighbour (triangulation sensors are associated with  
452 the nearest sensor from the skeletonization), b) an average, indicator by in-  
453 dicator, for each group of triangulation sensors associated with the same  
454 closest sensor from the skeletonization, c) a matching of the LCZ from the  
455 average with the LCZ calculated at the skeleton sensor.

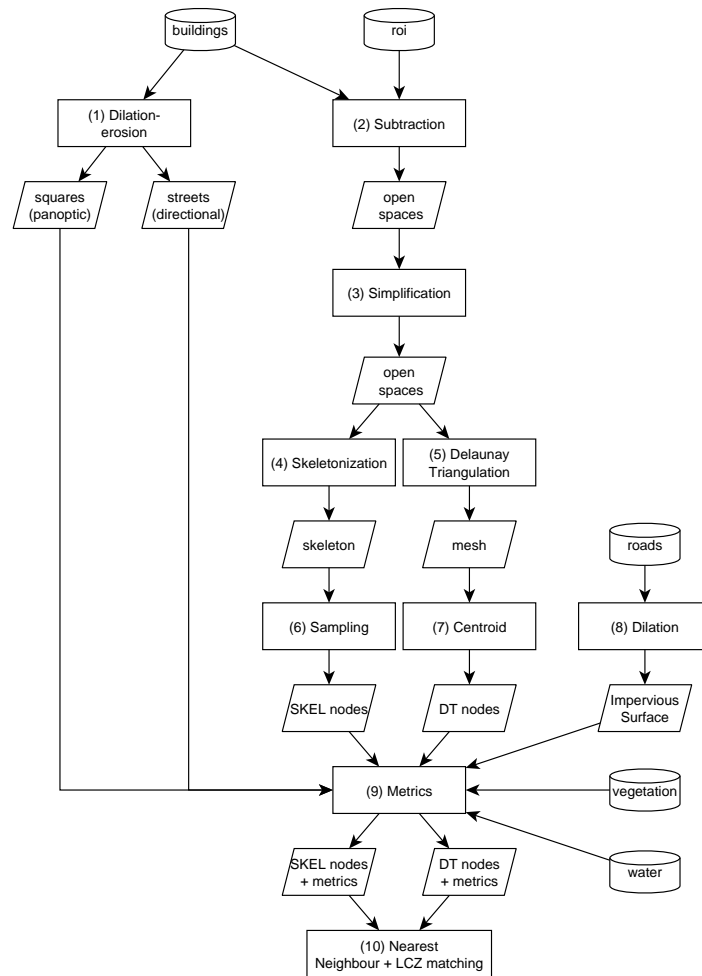


Fig. 9: The workflow implemented.

### 3 Results

456

457

458

459

460

461

462

463

464

In this section, three sensitivity studies are successively presented. The first concerns sensitivity to radius length. The second concerns the sensitivity to the number of rays used in the ray throwing mechanism. The third is a kind of sensitivity study of the type of sampling chosen. The number of variables and the related combinatorics being significant, we have arbitrarily chosen to present the most significant results. It should also be noted that the sensitivity studies presented in this section are a function of the spatial configuration of the selected urban fragments.

465

#### 3.1 Influence of radius length

466

467

A sensitivity analysis has been undertaken to know what impact the chosen radius length has on the accuracy of the sky view factor, the aspect

468 ratio, the building surface fraction, the impervious surface fraction, and the  
469 height of roughness elements (Fig. 10). Three radius were chosen: 50 m,  
470 100 m and 200 m. We can see on all districts that taking 100 m seems to be  
471 satisfactory on all calculated indicators: the median value is very close to  
472 the one obtained with a 200 m radius and the outliers are not too distant  
473 from the median, as with a 50 m radius.

474 The only indicator which is not influenced by the radius is the aspect  
475 ratio. It is quite easy to understand: the street width is most of the time  
476 not larger than 20 m so the first radius of 50 m already encompasses the  
477 street width and allows to hit the first built front. Therefore, the aspect  
478 ratio defined as the ratio between the height of the building and the street  
479 width will not change for these three radius.

480 The results presented in the following sections are all obtained with a  
481 100 m radius, which seemed to be a good compromise. Indeed, our objec-  
482 tive is not to reproduce a large-scale approach like the WUDAPT method,  
483 but to limit the range of the radius.

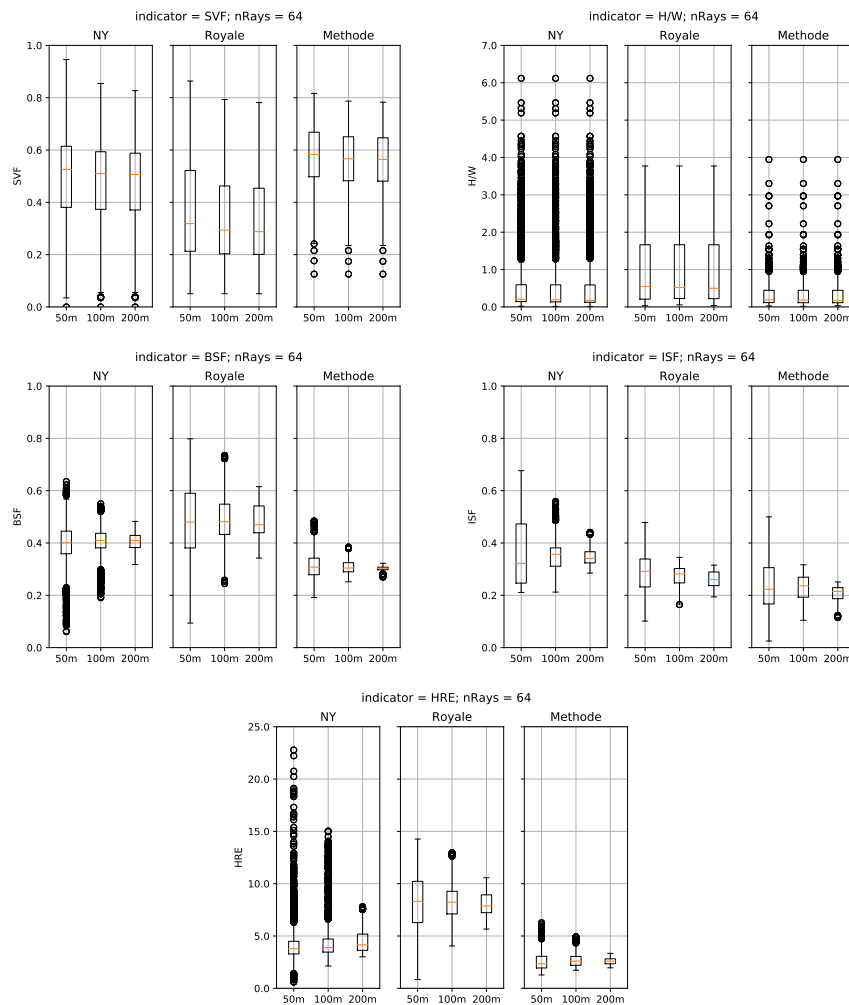


Fig. 10: Influence of the radius length on SVF, H/W, BSF, ISF, and HRE indicators, the number of rays being fixed at 64.

484

### 3.2 Influence of the number of rays

485

486

487

488

489

490

491

492

493

494

495

496

A sensitivity analysis has been undertaken to know what impact the chosen number of rays has on the accuracy of the five indicators - sky view factor, aspect ratio, building surface fraction, impervious surface fraction, and height of roughness elements (Fig. 11). Five different number of rays (ie. different angular abscissa values) were chosen: 16, 32, 64, 128, and 256. It is clear that, whatever the terrain chosen among the three, the increase in the number of rays does not significantly modify the values of all the indicators. In the following case studies, we arbitrarily set the number of rays at 64 (nRays). This angular abscissa value is a good compromise, since it allows an infra-decametric accuracy for a radius of 100 m while preserving a reasonable computation time, as we have been able to verify empirically in previous studies.

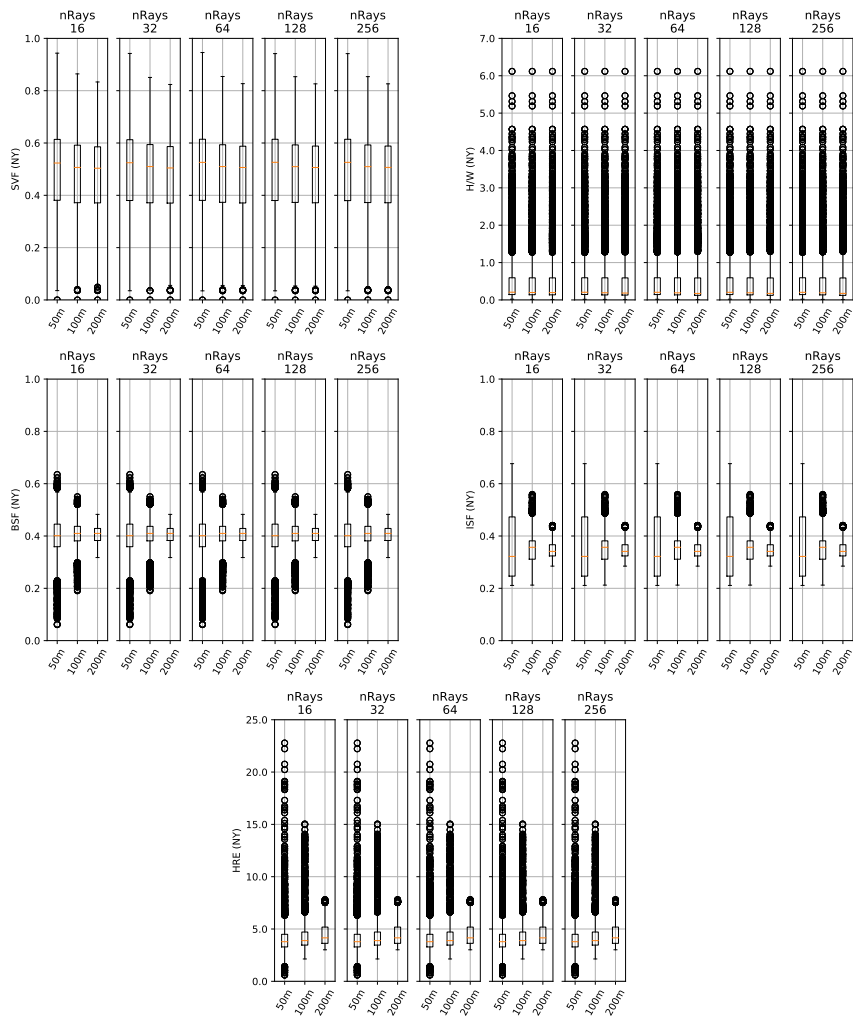


Fig. 11: Influence of the number of rays on SVF, H/W, BSF, ISF, and HRE indicators, the ray length being fixed at 100 m (Borough Park, New York).

497

### 3.3 LCZ - Delaunay Triangulation

498

499

500

501

502

503

504

505

506

507

508

509

The first figure (Fig. 12a) shows the identified LCZs on a district of New York. First of all, we can note that a lot of sensors are not identified within any LCZ. Second, we observe that the main LCZs are LCZ 2, 3 and 5 corresponding to compact high-rise, compact low-rise and open mid-rise. These first two LCZs are found both in the major and minor classes. Some sensors, in green, are identified as belonging to the open mid rise and low rise and very few, in blue, seem to belong to the lightweight low-rise class.

The second district located in Nantes (Royale) is mainly characterized by the LCZ 3 and 6 (Fig. 12b). Compared to Borough Park, this French district is less dense, with lower buildings, which is the reason why the LCZ found is lower than for Borough Park. Some outlying sensors are identified as LCZ 3 and 5. Finally, this district is mainly compact low-rise

510  
511  
512  
513  
514  
515  
516  
517  
518  
519  
520  
521  
522  
523  
524  
525

and open mid-rise.

The Méthode district of Nantes has a lot of **non-identified** sensors, because they do not match within any of the LCZs proposed by (I. D. Stewart and T. R. Oke 2012) (Fig. 12c). Close to the higher buildings, LCZ 3 is found and LCZ 5 and 6 are found. Most of the minors are identified as LCZ 6. This shows that Méthode district is less compact and low-rise compared to the Royale district.

Not all nodes of the districts studied in this paper are associated to a LCZ. There is a clear difference between the typical urban configuration of a North American district with contemporary architecture, where only 24% of the nodes do not match to a LCZ and the classic European architectural district of Royale, where 34.7% of the nodes have no associated LCZ. Finally for Méthode, a residential area of intermediate density, the worst case, 83.7% of the nodes do not meet the requirements to fit to a LCZ. These results show clearly that the LCZ classification is better suited to the dense and planned urban districts than to the classical or diffused ones.

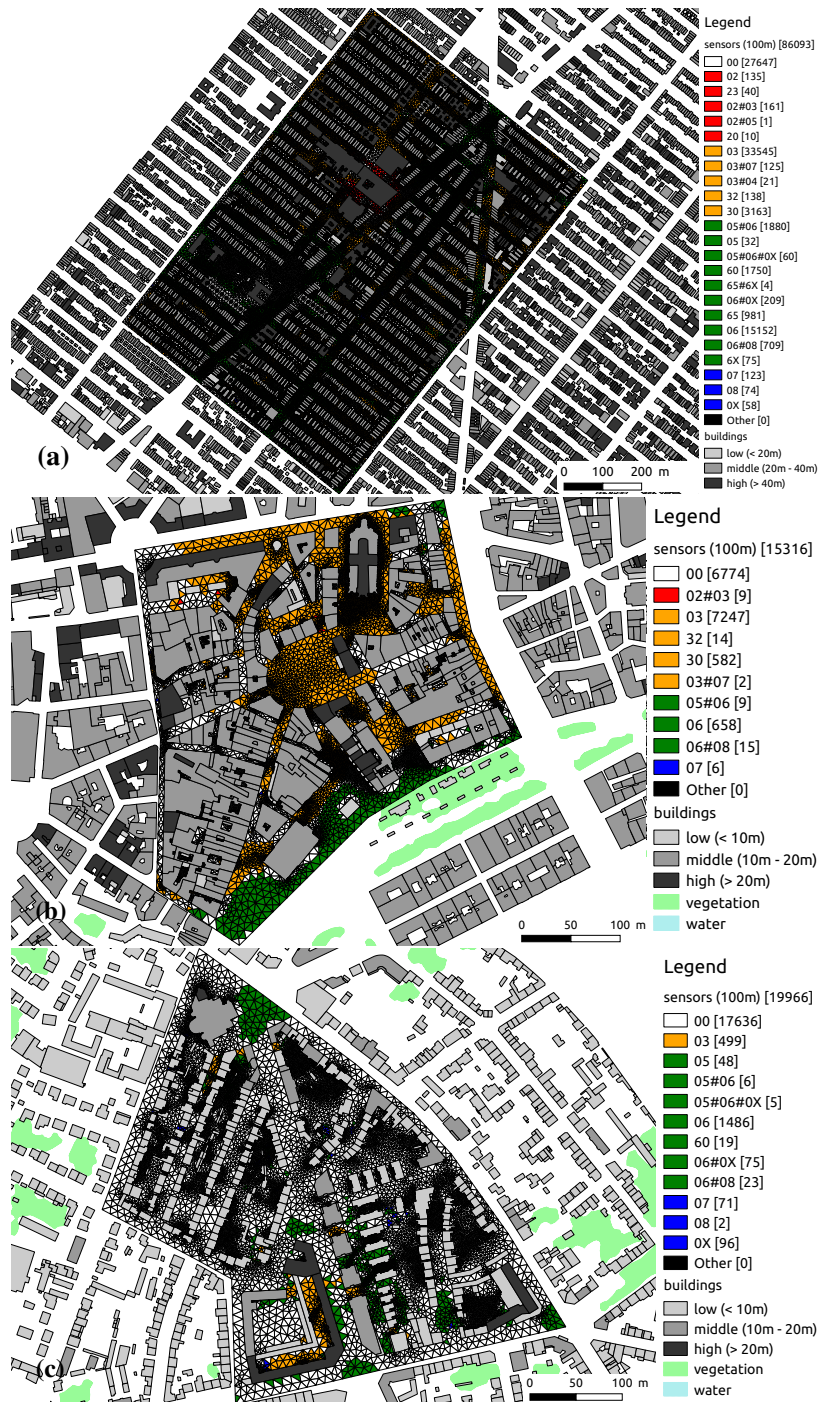


**Fig. 12:** Determination of LCZs for the three case studies (Delaunay Triangulation, rayLen=100m, nRays=64): (a) New York (Borough Park). (b) Nantes, France (Royale district). (c) Nantes, France (Méthode district).

526

### 3.4 LCZ - skeleton

527

The main observations for all districts are similar to the ones obtained with the Delaunay triangulation method (Fig. 13).

528

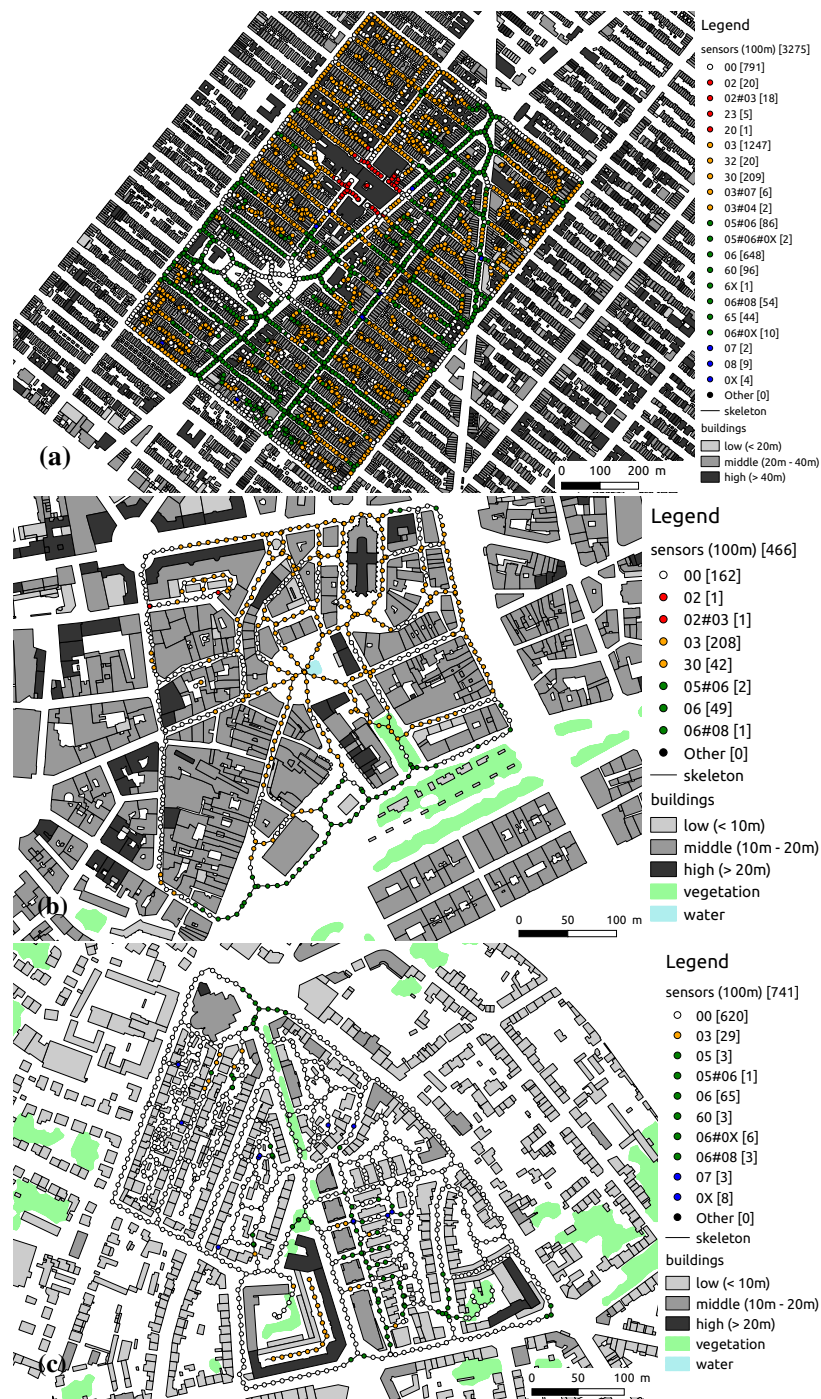


**Fig. 13:** Determination of LCZs for the three case studies (Skeleton, rayLen=100m, nRays=64): (a) New York (Borough Park). (b) Nantes, France (Royale district). (c) Nantes, France (Méthode district).

530 a district of New York (Fig. 13a). Again, the main LCZs are LCZ 2, 3 and 5,  
531 corresponding to compact high-rise and compact low-rise.

532 The second district located in Nantes (Royale) is again mainly charac-  
533 terized by the LCZ 3 and 6 (Fig. 13b) and the same outlying sensors.

534 The Méthode district of Nantes has again a lot of non-identified sensors  
535 because they do not match into any of the LCZs proposed by (I. D. Stewart  
536 and T. R. Oke 2012) (Fig. 13c) and close to the higher buildings, LCZ 3 is  
537 found and LCZ 5 and 6 are found too.

### 538 3.5 Verification of the LCZ simulated

539 A local climate zone is defined as an area which presents uniform fea-  
540 tures as for example in terms of urban morphology, land use, and a charac-  
541 teristic screen-height temperature regime. This is why we have first com-  
542 pared the LCZ obtained in this paper to the air temperature measured by  
543 (Bernard, Musy, et al. 2017). First, we have observed a distinct air temper-  
544 ature difference between Royale district and Méthode district. (Bernard,  
545 Musy, et al. 2017) observed an UHI amplitude of 2.5° C in the Royale dis-  
546 trict and an amplitude of 1.5° C only for Méthode district. This means that  
547 between Royale district and Méthode district the air temperature differ-  
548 ence is of one degree. This confirms our results: the two districts do not  
549 belong to the same LCZ as their air temperature regime is not the same.

550 Secondly, we have compared the LCZ obtained on Royale district and  
551 Méthode district to the LCZ map of WUDAPT community<sup>6</sup>. The tenden-  
552 cies are verified: Royale district is classified as LCZ 3 by WUDAPT and  
553 corresponds to the major LCZ found in this paper. Méthode district is clas-  
554 sified as LCZ 6 by WUDAPT and corresponds to the major LCZ found in  
555 this paper. This last verification is very global as the WUDAPT LCZ map is  
556 only one hundred meter per one hundred meter large. Unfortunately, this  
557 resolution is not accurate enough to validate the minor LCZ found in this  
558 paper. To improve the validation at a smaller scale, air temperature sensors  
559 should have been placed in the urban open spaces of Royale and Méthode  
560 districts. This could not be done in the context of this study paper due to  
561 the lack of funding, but should be done in future.

### 562 3.6 About calculation times

563 We performed all the simulations on a Linux Ubuntu 14.04 LTS com-  
564 puter, equipped with Intel® Xeon® Processor E3-1246 v3 (Quad Core HT,  
565 3.50GHz, 8MB) and with 16Go 1600MHz DDR3 Non-ECC SDRAM. The  
566 version of the QGIS software used is 2.18.11, the version of the GMSH soft-  
567 ware used to mesh the study space is 2.8.3.

568 For the estimation of calculation times, we take care to clearly distin-  
569 guish pre-processing (by Delaunay triangulation or skeletonization), pro-  
570 cessing (evaluation of indicators and LCZ in each sensor), and post-processing  
571 (matching of the two methods, mapping rendering). The calculation times  
572 given in Table 3 correspond only to the processing times, excluding pre-  
573 and post-processing.

---

<sup>6</sup>See the map available at [https://geopedia.world/#T4\\_L107\\_x-168925.83251023944\\_y5992280.832416391\\_s10\\_b17](https://geopedia.world/#T4_L107_x-168925.83251023944_y5992280.832416391_s10_b17) (Accessed February 2019).

Table 3: Calculation times (hh:mm:ss).

Mesh type	District	Number of sensors	Ray lengths (m)		
			50	100	200
Triangulated Irregular Network	New York Borough Park	86,093	03:44:42	05:07:21	14:13:02
	Nantes Royale district	15,316	00:20:19	00:48:44	02:15:12
	Nantes Méthode district	19,966	00:20:46	00:52:51	02:30:59
Skeleton	New York Borough Park	3275	00:07:39	00:12:50	00:31:19
	Nantes Royale district	466	00:00:37	00:01:21	00:03:54
	Nantes Méthode district	741	00:00:46	00:01:52	00:05:52

574 As an indication, we can specify that the pre-processing time for Bor-  
575 ough Park (New York) is 00:37:59 with the Skeletonization and 00:04:46  
576 with the Triangulation. The pre-processing time for the Royale District  
577 (Nantes) is 00:00:26 (Skeletonization) and 00:00:13 (Triangulation). The pre-  
578 processing time for Méthode District (Nantes) is 00:00:28 (Skeletonization)  
579 and 00:00:19 (Triangulation). The pre-processing time for Skeletonization  
580 is always longer than for the triangulation as seen above, but it is for the  
581 processing times Table 3 that the Skeletonization becomes very interesting  
582 compared to the Delaunay triangulation. For example, for New York and  
583 with a ray length of 100 m the skeleton needs  $\leq 13$  min, whereas the trian-  
584 gulated network needs more than five hours to process.

## 585 4 Discussion

### 586 4.1 LCZs correlation

587 The figures below show the correlation between the results obtained  
588 with the Delaunay triangulation and the skeletonization (Fig. 14). The con-  
589 fidence interval is set to one when results are entirely correlated, and set to  
590 zero when no correlation is found as explained before.

591 For New York, 2817 sensors out of 3270 (86.1%) have a very high confi-  
592 dence interval and 447 sensors out of 3270 (13.7%) have a good confidence.

593 For the Royale district, 359 out of 465 sensors have a high confidence  
594 interval, which represents (77.2%) of high confident sensors.

595 Third, the Méthode District presents 654 sensors out of the 739 total  
596 sensors, which have a confidence between 0.82 and 1, which represents  
597 88.5%.

598 To conclude, most of the sensors of the three districts show a high con-  
599 fidence between 0.82 and 1. This means that the skeleton is representative  
600 of the district and can be applied to predict the local climate zones.

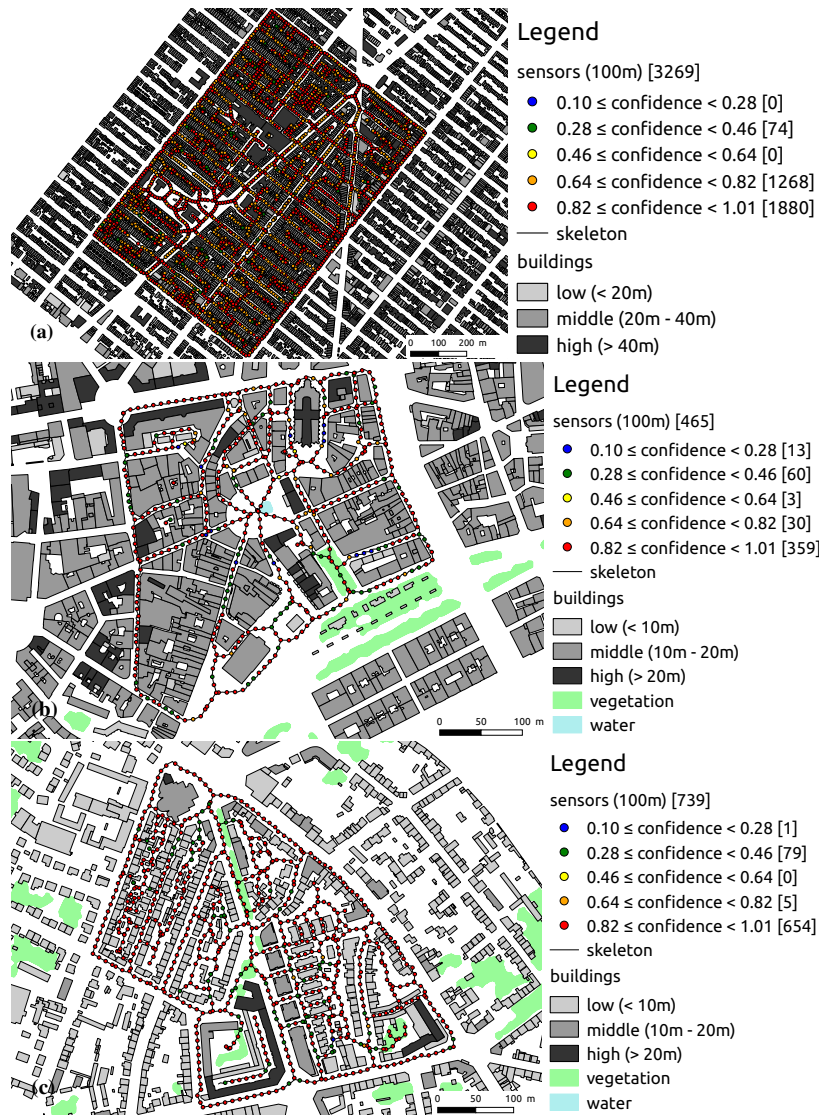


Fig. 14: LCZs correlation: Delaunay Triangulation vs. Skeleton, for the three case studies (rayLen=100m): (a) New York (Borough Park). (b) Nantes, France (Royale district). (c) Nantes, France (Méthode district).

## 4.2 Indeterminacy of LCZs: Zoom in nodata values

601  
602  
603  
604  
605  
606  
607  
608  
609

The street of "rue d'Orléans" in Nantes opens to the west on Place Royale and to the east on the courtyard named "50 otages" (Fig. 15a). This street is a pedestrian zone made up of a homogeneous group of buildings of classic style. Unlike the sensors at its ends - which fall exclusively under LCZ 3 - the 24 "central" sensors on this street do not fit into any LCZ (white facets). This indetermination can be attributed to two of the five indicators allowing the identification of the associated LCZ. Therefore, if, for these 24 sensors, the BSF, ISF and HRE come under LCZ 3, a contrario, on this

610 zone, the values of SVF spread between 17.31% and 19.37%, and those of  
611 H/W spread between 1.66 and 1.84. According to (I. D. Stewart and T. R.  
612 Oke 2012), the thresholds for the SVF and H/W indicators in LCZ 3 are  
613 set between 20% and 60% on the one hand, and 0.75 and 1.5 on the other.  
614 We conclude that, for these thresholds and for our indicator calculation  
615 method, this street is too "boxed/canyon" to fit into LCZ 3.

616 The 27 sensors located in the lower part of the "rue du Chapeau Rouge"  
617 are in a situation of indeterminacy (Fig. 15b), while the sensors surround-  
618 ing them are registered in LCZ 2 or 3. To explain this indeterminacy, we  
619 analyzed the values of all the indicators of each of these sensors. In all  
620 cases, it appears that, in all cases, the SVF indicator places the sensors in  
621 LCZ 2 as in LCZ 3, the indicator places the sensors in LCZ 2 as in LCZ 3  
622 (but also in LCZ 1), the ISF indicator places the sensors in LCZ 3 (but also  
623 in LCZ 6 and 10), the HRE indicator places the sensors in LCZ 2 (but also in  
624 LCZ 5 and 10). In addition, in a majority of cases, the h/w indicator places  
625 a majority of the sensors in LCZ 5 or 6 (but in no case in LCZ 2 or LCZ 3).  
626 If three indicators (SVF, BSF, and HRE) place all the sensors in LCZ 2 and  
627 three indicators (SVF, BSF and ISF) place them in LCZ 3, one can notice that  
628 there is no LCZ for these sensors that has at least 4 of the 5 indicators. This  
629 lack justifies the indeterminacy we see when we read the map.

630 As in the case of "rue d'Orléans", the 24 sensors on "rue des Vieilles  
631 Douves" (Fig. 15c) - which opens to the west northwest into the Place Royale  
632 - are undetermined. This indeterminacy is all the more surprising as, on  
633 both sides, the sensors are exclusively under LCZ 3. A more precise study  
634 allows us to attribute this indeterminacy only to the SVF and h/w indi-  
635 cators (BSF, ISF, and HRE being perfectly in line with LCZ 3). Indeed,  
636 for these sensors, the SVF values spread between 6.23% and 19.79% and  
637 those of h/w spread between 1.58 and 3.83. We are well below 20% in the  
638 first case, and above 1.5 in the second. More than "rue d'Orléans", "rue des  
639 Vieilles Douves" is far too "boxed/canyon" to fit into LCZ 3.

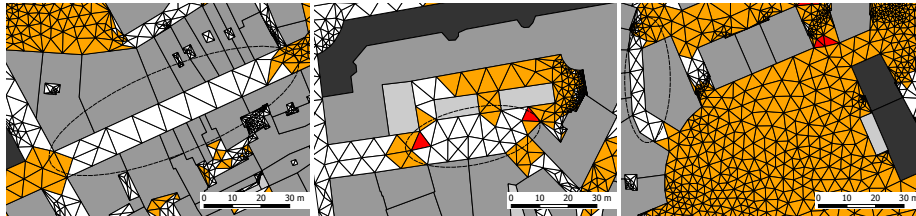


Fig. 15: Three cases of indeterminacy: (a) rue d'Orléans. (b) rue du Chapeau Rouge.(c) rue des Vieilles Douves.

640 We can conclude that the intervals proposed by (I. D. Stewart and T. R.  
641 Oke 2012) are not covering perfectly all the potential indicator values as  
642 seen here.

## 643 5 Conclusion and outlooks

644 This paper presents a methodology to apply local climate zones classi-  
645 fication on local and micro scales. Among seven indicators proposed by  
646 (I. D. Stewart and T. R. Oke 2012), corresponding to geometric and surface  
647 cover properties, five have been implemented successfully in this paper.

648 Two indicators among these five have been improved. A SVF definition  
649 adapted from (Bernard, Bocher, et al. 2018) has been implemented in our  
650 paper. The aspect ratio is calculated differently either for canyon streets or  
651 squares. This distinction is related to the lack of a clear main direction for  
652 open spaces that are not canyons.

653 The advantage of the proposed method is that the generation of LCZs  
654 is repeatable elsewhere providing that the standard geographical information  
655 of the city is given. Another advantage of the proposed method is  
656 that it is robust: the major and minor LCZs found follow a deterministic  
657 algorithm transposable elsewhere.

658 After a sensitivity analysis on the radius length, the results on several  
659 districts showed that the indicators could be calculated for different meth-  
660 ods of dividing the space: the Delaunay triangulation and the Skeletoniza-  
661 tion. Results obtained with Skeletonization are strongly correlated to De-  
662 launay's, which means that skeletonization could replace the Delaunay  
663 triangulation. Skeletonization showed also the advantage to pull down  
664 calculation time. The major LCZs found on the districts of Nantes are com-  
665 pared to previous obtained UHI measures and to WUDAPT portal. These  
666 comparisons confirm that the major LCZs found in this paper are coherent.

667 Finally, we observe that some sensors are not identified within any LCZ,  
668 or aligned poorly with a LCZ. A first reason is, that there is no LCZ for  
669 these sensors that validates at least 4 of the 5 indicators. For another case,  
670 three indicators come into a LCZ but the two remaining indicators do not  
671 fit into any LCZ. This means that the local climate zones proposed by (I. D.  
672 Stewart and T. R. Oke 2012) do not cover all the urban fabrics as for ex-  
673 ample the more classic architecture and is more suited to contemporary  
674 urban forms as already highlighted by (Leconte et al. 2015). In the future,  
675 the classification propose by (I. D. Stewart and T. R. Oke 2012) needs to be  
676 improved, so that more urban fabrics can be identified and classified into  
677 a local climate zone. We propose to continue working on LCZ subclasses  
678 as some authors have already done (Kotharkar and Bagade 2018; Leconte  
679 et al. 2015). But the main challenge is still to identify the main urban fab-  
680 rics that do not fit into the LCZ proposed by (I. D. Stewart and T. R. Oke  
681 2012) as for example some regions of the city of Nancy which present im-  
682 portant inhomogeneities in surface structure cover, fabric, etc. (Leconte et  
683 al. 2015). Once a set of **non-identified** regions are put aside we propose to  
684 measure the air temperature within these regions and identify the vulnera-  
685 bility of these regions to the UHI magnitude. Then, we propose to retrieve  
686 the urban indicators representing these regions. After that, we propose to  
687 add these new LCZs (characterized by the urban indicators representing  
688 them) to the classical LCZ scale (I. D. Stewart and T. R. Oke 2012). Finally  
689 the modified LCZ scale should improve the estimation of the UHI magni-  
690 tude for heterogeneous and compact cities. Moreover, the albedo needs to  
691 be identified and considered when looking for the LCZ. The consideration  
692 of the albedo is proposed by (I. D. Stewart and T. R. Oke 2012) but has  
693 not been calculated in our paper, which should be done in the future. The  
694 identification of the albedo at a district scale is challenging, though some  
695 authors found a simpler method to evaluate the urban albedo at a block  
696 scale (Bernabé et al. 2015).

697 A future work will be to obtain the air temperature in the districts pre-  
698 sented in this paper using mobile measurements to confirm the major and  
699 minor LCZs found. This validation will be done on a smaller scale, com-  
700 pared to the global verification done in this paper.

## 701 Acknowledgments

702 ...

## 703 Conflict of interests

704 The authors declare no conflict of interest.

## 705 Abbreviations

706 The following abbreviations are used in this manuscript:

707  
708 BSF: Building Surface Fraction  
709 DT: Delaunay Triangulation  
710 HRE: Height of Roughness Elements  
711 LCZ: Local climate zone  
712 PSF: Pervious Surface Fraction  
713 ROI: Region Of Interest  
714 SKEL: Skeleton  
715 SVF: Sky View Factor  
716 UHI: Urban Heat Island  
717 WUDAPT: World Urban Database and Access Portal Tools  
718

## 719 References

- 720 Azam, Marie-Hélène et al. (2018). "A pavement-watering thermal  
721 model for SOLENE-microclimat: **Development** and evaluation".  
722 In: Urban Climate vol. 25, pp. 22–36. ISSN: 22120955. DOI: 10 .  
723 1016 / j . uclim . 2018 . 04 . 005. URL: [https://linkinghub.  
724 elsevier.com/retrieve/pii/S2212095518301159](https://linkinghub.elsevier.com/retrieve/pii/S2212095518301159).
- 725 Bechtel, Benjamin et al. (2017). "Quality of Crowdsourced **data on**  
726 **urban morphology** - The **human influence experiment** (HUMINEX)".  
727 In: Urban Science 1.2, p. 15. ISSN: 2413-8851. DOI: 10 . 3390 /  
728 urbansci1020015. URL: [http://www.mdpi.com/2413-8851/  
729 1/2/15](http://www.mdpi.com/2413-8851/1/2/15).
- 730 Benedikt, **Michael L.** (1979). "To take hold of space: isovists and iso-  
731 vist fields". In: Environment and Planning B: Planning and Design  
732 6.1, pp. 47–65. DOI: 10.1068/b060047. URL: [https://journals.  
733 sagepub.com/doi/abs/10.1068/b060047](https://journals.sagepub.com/doi/abs/10.1068/b060047).
- 734 Bernabé, Anne et al. (2015). "Radiative properties of the urban fab-  
735 ric derived from surface form analysis: A simplified solar bal-  
736 ance model". In: Solar Energy 122, pp. 156–168. ISSN: 0038092X.  
737 DOI: 10 . 1016 / j . solener . 2015 . 08 . 031. URL: [https://  
738 linkinghub.elsevier.com/retrieve/pii/S0038092X15004673](https://linkinghub.elsevier.com/retrieve/pii/S0038092X15004673).

- 739 Bernard, Jérémy, Erwan Bocher, et al. (2018). "Sky view factor cal-  
740 culation in urban context: Computational performance and ac-  
741 curacy analysis of two open and free GIS tools". In: *Climate* 6.3,  
742 p. 60. ISSN: 2225-1154. DOI: 10.3390/cli6030060. URL: <http://www.mdpi.com/2225-1154/6/3/60>.  
743
- 744 Bernard, Jérémy, Marjorie Musy, et al. (2017). "Urban heat island  
745 temporal and spatial variations: Empirical modeling from geo-  
746 graphical and meteorological data". In: *Building and Environment*  
747 125, pp. 423–438. ISSN: 03601323. DOI: 10.1016/j.buildenv.  
748 2017.08.009. URL: [https://linkinghub.elsevier.com/  
749 retrieve/pii/S0360132317303554](https://linkinghub.elsevier.com/retrieve/pii/S0360132317303554).
- 750 Bernard, Jérémy, Auline Rodler, et al. (2018). "How to design a park  
751 and its surrounding urban morphology to optimize the spread-  
752 ing of cool air?" In: *Climate* 6.1, p. 10. ISSN: 2225-1154. DOI:  
753 10.3390/cli6010010. URL: [http://www.mdpi.com/2225-  
754 1154/6/1/10](http://www.mdpi.com/2225-1154/6/1/10).
- 755 Bocher, Erwan et al. (2018). "A geoprocessing framework to com-  
756 pute urban indicators: The MApUCE tools chain". In: *Urban Climate*  
757 24.January, pp. 153–174. ISSN: 22120955. DOI: 10.1016/j.uclim.  
758 2018.01.008.
- 759 Fenner, Daniel et al. (2017). "Intra and inter 'local climate zone' vari-  
760 ability of air temperature as observed by crowdsourced citizen  
761 weather stations in Berlin, Germany". In: *Meteorologische Zeitschrift*  
762 26.5, pp. 525–547. ISSN: 16101227. DOI: 10.1127/metz/2017/  
763 0861.
- 764 Gál, Tamás, F. Lindberg, and J. Unger (2009). "Computing continu-  
765 ous sky view factors using 3D urban raster and vector databases:  
766 Comparison and application to urban climate". In: *Theoretical and Applied Climatology*  
767 95.1-2, pp. 111–123. ISSN: 0177-798X. DOI: 10.1007/s00704-  
768 007-0362-9. URL: [http://link.springer.com/10.1007/  
769 s00704-007-0362-9](http://link.springer.com/10.1007/s00704-007-0362-9).
- 770 Geletič, Jan and Michal Lehnert (2016). "GIS-based delineation of  
771 local climate zones: The case of medium-sized central European  
772 cities". In: *Moravian Geographical Reports* 24.3, pp. 2–12. ISSN:  
773 12108812. DOI: 10.1515/mgr-2016-0012. URL: [http://content.  
774 sciendo.com/view/journals/mgr/24/3/article-p2.xml](http://content.sciendo.com/view/journals/mgr/24/3/article-p2.xml).
- 775 Grimmond, C. S. B. et al. (2010). "The International Urban Energy  
776 Balance Models Comparison Project: First Results from Phase  
777 1". In: *Journal of Applied Meteorology and Climatology* 49.6, pp. 1268–  
778 1292. ISSN: 1558-8424. DOI: 10.1175/2010JAMC2354.1. URL:  
779 [http://journals.ametsoc.org/doi/abs/10.1175/2010JAMC2354.  
780 1](http://journals.ametsoc.org/doi/abs/10.1175/2010JAMC2354.1).
- 781 Johnson, Glenn T. and Ian D. Watson (1984). "The Determination of  
782 View-Factors in Urban Canyons". In: *Journal of Climate and Applied Meteorology*  
783 23.2, pp. 329–335. ISSN: 0733-3021. DOI: 10.1175/1520-0450(1984)  
784 023<0329:TDOVFI>2.0.CO;2. URL: [http://journals.ametsoc.  
785 org/doi/abs/10.1175/1520-0450%7B%7D281984%7B%  
786 %7D29023%7B%7D3C0329%7B%7D3ATDOVFI%7B%7D3E2.0.  
787 CO%7B%7D3B2](http://journals.ametsoc.org/doi/abs/10.1175/1520-0450%7B%7D281984%7B%7D29023%7B%7D3C0329%7B%7D3ATDOVFI%7B%7D3E2.0.CO%7B%7D3B2).

- 788 Kotharkar, Rajashree and Anurag Bagade (2018). "Evaluating ur-  
789 ban heat island in the critical local climate zones of an Indian  
790 city". In: *Landscape and Urban Planning* 169, pp. 92–104. ISSN:  
791 01692046. DOI: 10.1016/j.landurbplan.2017.08.009. URL:  
792 [https://content.sciencedirect.com/view/journals/mgr/24/3/  
793 article-p2.xml](https://content.sciencedirect.com/view/journals/mgr/24/3/article-p2.xml).
- 794 Lai, Li Wei (2018). "The influence of urban heat island phenomenon  
795 on PM concentration: An observation study during the summer  
796 half-year in metropolitan Taipei, Taiwan". In: *Theoretical and Applied Climatology*  
797 131.1-2, pp. 227–243. ISSN: 14344483. DOI: 10.1007/s00704-  
798 016-1975-7.
- 799 Leconte, Francois et al. (2015). "Using local climate zone scheme for  
800 UHI assessment: Evaluation of the method using mobile mea-  
801 surements". In: *Building and Environment* 83, pp. 39–49. ISSN:  
802 03601323. DOI: 10.1016/j.buildenv.2014.05.005.
- 803 Lelovics, E et al. (2014). "Design of an urban monitoring network  
804 based on local climate zone mapping and temperature pattern  
805 modelling". In: *Climate Research* 60.1, pp. 51–62. ISSN: 0936-577X.  
806 DOI: 10.3354/cr01220.
- 807 Mills, Gerald (2007). "Cities as agents of global change". In: *International Journal of Climatology*  
808 27.14, pp. 1849–1857. ISSN: 08998418. DOI: 10.1002/joc.1604.  
809 URL: <http://doi.wiley.com/10.1002/joc.1604>.
- 810 Morille, Benjamin and Marjorie Musy (2017). "Comparison of the  
811 impact of three climate adaptation strategies on summer ther-  
812 mal comfort - cases study in Lyon, France". In: *Procedia Environmental Sciences*  
813 38, pp. 619–626. ISSN: 18780296. DOI: 10.1016/j.proenv.2017.  
814 03.141. URL: [http://linkinghub.elsevier.com/retrieve/  
815 pii/S1878029617301457](http://linkinghub.elsevier.com/retrieve/pii/S1878029617301457).
- 816 Musy, Marjorie, Laurent Malys, and Christian Inard (2017). "As-  
817 sessment of direct and indirect impacts of vegetation on build-  
818 ing comfort: A comparative study of lawns, green walls and  
819 green roofs". In: *Procedia Environmental Sciences* 38, pp. 603–  
820 610. ISSN: 18780296. DOI: 10.1016/j.proenv.2017.03.134.  
821 URL: [http://linkinghub.elsevier.com/retrieve/pii/  
822 S187802961730138X](http://linkinghub.elsevier.com/retrieve/pii/S187802961730138X).
- 823 Musy, Marjorie, Laurent Malys, Benjamin Morille, et al. (2015). "The  
824 use of SOLENE-microclimat model to assess adaptation strate-  
825 gies at the district scale". In: *Urban Climate* 14.March 2016, pp. 213–  
826 223. ISSN: 22120955. DOI: 10.1016/j.uclim.2015.07.004.  
827 URL: [http://linkinghub.elsevier.com/retrieve/pii/  
828 S2212095515300109](http://linkinghub.elsevier.com/retrieve/pii/S2212095515300109).
- 829 Oke, Tim R. (2006). "Towards better scientific communication in  
830 urban climate". In: *Theoretical and Applied Climatology*. ISSN:  
831 14344483. DOI: 10.1007/s00704-005-0153-0.
- 832 Oke, T.R. (1987). *Boundary Layer Climates, 2nd edition*. Routledge.  
833 ISBN: 9780415043199.
- 834 — (1988). "Street design and urban canopy layer climate". In: *Energy and Buildings*  
835 11.1-3, pp. 103–113. ISSN: 03787788. DOI: 10.1016/0378-7788(88)  
836 90026-6. URL: [http://linkinghub.elsevier.com/retrieve/  
837 pii/0378778888900266](http://linkinghub.elsevier.com/retrieve/pii/0378778888900266).

838  
839  
840  
841  
842  
843  
844  
845  
846  
847  
848  
849  
850  
851  
852  
853  
854  
855  
856  
857  
858  
859  
860  
861  
862  
863  
864  
865  
866  
867  
868  
869  
870  
871  
872  
873  
874  
875  
876  
877  
878  
879  
880  
881  
882  
883  
884

- Openshaw, Stan (1983). "The modifiable areal unit problem". In: CATMOG - Concepts and Techniques in Modern Geography vol. 38, p. 41. URL: <http://www.getcited.org/pub/102412488>.
- Perera, N.G.R and R. Emmanuel (2018). "A "local climate zone" based approach to urban planning in Colombo, Sri Lanka". In: Urban Climate 23, pp. 188–203. ISSN: 22120955. DOI: 10.1016/j.uclim.2016.11.006.
- Plumejeaud-Perreau, Christine et al. (2015). "Building local climate zones by using socio-economic and topographic vectorial databases". In: ICUC9, Toulouse, France (20-24 July).
- Quanz, Justus A et al. (2018). "Micro-scale variability of air temperature within a local climate zone in Berlin, Germany, during summer". In: Climate 6.1, p. 5. ISSN: 2225-1154. DOI: 10.3390/cli6010005. URL: <http://www.mdpi.com/2225-1154/6/1/5>.
- Salvati, Agnese, Helena Coch Roura, and Carlo Cecere (2015). "Urban morphology and energy performance: The direct and indirect contribution in Mediterranean climate". In: PLEA 2015 Architecture in (R)Evolution - 31st Inter pp. 1–8.
- Santamouris, M. et al. (2017). "Passive and active cooling for the outdoor built environment - analysis and assessment of the cooling potential of mitigation technologies using performance data from large scale projects". In: Solar Energy 2017, pp. 154, 14–33.
- Sarradin, François et al. (2007). "Comparing sky shape skeletons for the analysis of visual dynamics along routes". In: Environment and Planning B: Planning and Design 34.5, pp. 840–857. ISSN: 0265-8135. DOI: 10.1068/b32143. URL: <http://journals.sagepub.com/doi/10.1068/b32143>.
- Souza, Léa C.L., Daniel S. Rodrigues, and José F.G. Mendes (2003). "Sky view factors estimation using a 3D-GIS extension". In: 8th International IBPSA Conference, pp. 1227–1234. URL: <http://hdl.handle.net/1822/2206>.
- Stewart, I. D. and T. R. Oke (2012). "Local climate zones for urban temperature studies". In: American Meteorological Society.
- Stewart, Iain D., T. R. Oke, and E. Scott Krayenhoff (2014). "Evaluation of the 'local climate zone' scheme using temperature observations and model simulations". In: International Journal of Climatology 34.4, pp. 1062–1080. ISSN: 08998418. DOI: 10.1002/joc.3746.
- Steyn, D.G. (1980). "The calculation of view factors from fisheye-lens photographs: Research note". In: Atmosphere-Ocean 18.3, pp. 254–258. ISSN: 0705-5900. DOI: 10.1080/07055900.1980.9649091.
- Teller, Jacques and S. Azar (2001). "Townscope II-A computer system to support solar access decision-making". In: Solar Energy 70.3, pp. 187–200. ISSN: 0038092X. DOI: 10.1016/S0038-092X(00)00097-9. URL: <http://linkinghub.elsevier.com/retrieve/pii/S0038092X00000979>.
- Yu, Bingfeng et al. (2008). "Study on the influence of albedo on building heat environment in a year-round". In: Energy and Buildings 40, pp. 945–951.